Micro-Raman and X-ray Photoemission Spectroscopic Investigations of Heterojunction Between Delafossite CuGaO2 and Wurtzite ZnO Obtained by Hydrothermal Method

Minuk Choi

Nagoya Institute of Technology

Christoph Brabec

University of Erlangen-Nuremberg

Tomokatsu Hayakawa (✉ hayatomo@nitech.ac.jp)

Nagoya Institute of Technology

Research Article

Abstract

P-type delafossite CuGaO2 is a wide-bandgap semiconductor for optoelectronic applications, and its lattice parameters are very similar to those of n-type semiconductor wurtzite ZnO. Therefore, the investigation on p-n junction properties of crystalline CuGaO2 /ZnO heterostructures has attracted significant attention. In this study, interfacial CuGaO2 /ZnO heterojunctions were examined through X-ray diffraction (XRD) analysis, confocal micro-Raman spectroscopy, and X-ray photoelectron spectroscopy (XPS). XRD analysis revealed that the hydrothermal deposition of ZnO on hexagonal platelet CuGaO2 base crystals was successful, and the subsequent reduction process could induce a unique reaction between CuGaO2 and ZnO. XPS allowed the comparison of the binding energies (peak position and width) of the valence electrons of the constituents (Cu, Ga, (Zn) and O) of the pristine CuGaO2 single crystallites and of crystalline CuGaO2 /ZnO heterojunctions. The presence of distorted GaO6 octahedra at the CuGaO2 /ZnO hybrid interface and the absence of Cu2+ ions were the main characteristics of the chemically well-reconstructed heterojunction interface that facilitated effective carrier separation.

Introduction

The development of semiconducting materials that can produce hydrogen,[1] decompose organic pollutants,[2] and improve power generation efficiency[3] toward environmental purification and energy management is a growing research field that has received significant attention from material chemists as well as device manufacturers.[4,5] It is well known that in a hybrid p-n junction with different types of semiconductors having opposite carrier transport characteristics, band bending of the electronic structure occurs at the interface between the semiconductors.[6] In an n-type semiconductor, as shown in **Fig. 1 (i)**, electrons excited in the conduction band enter the semiconductor because of the potential slope generated by band bending, and the holes in the valence band move to the adjacent semiconductor interface. In contrast, photogenerated holes in the p-type semiconductor remain in the interior, whereas electrons move toward the interface and arrive at the adjacent semiconductor (see **Fig. 1(ii)**). The continuous excitation of electron−hole pairs is also possible at the interface; consequently, electrons and holes are effectively separated by the steep slope of the band potentials.[7,8] In this case, a redox reaction is expected on each surface (involving electrons and holes on the n- and p-type sides, respectively) when semiconductor heterostructures act as catalysts under light illumination above the band-gap energy (see **Fig. 1(iii)**).

Copper-based delafossite-type oxides with a composition of $CuMO_2$ (M = Al, Ga, Cr) have been studied as new p-type semiconductors because of their high hole mobility, nontoxicity, high abundance, environmental friendliness, and low cost.[9]

Delafossite-type oxide copper gallate ($CuGaO_2$) has a rhombohedral (3R) or hexagonal (2H) symmetry, with a layer of GaO_6 octahedra sandwiched between successive O−Cu−O layers. The valence band is composed of an electronic hybrid of the 3d orbital of Cu atoms and the 2p orbital of O atoms, which is delocalized by oxygen atoms and forms at a low energy level. In addition, Cu vacancies and interstitial O

atoms can produce holes, resulting in p-type conductivity. As a wide-band-gap semiconductor, $CuGaO_2$ possesses a direct band gap at a high energy of 3.4–3.7 eV and a small absorption tail starting at 2 eV due to an indirect band gap,[10] which enables its applications in p-n junction devices, p-type dye-sensitized solar cells, and photocatalysts.[11–13] Ehara[14] successfully fabricated transparent delafossite-type $CuGaO_2$ thin films for dye-sensitized solar cells by a sol−gel method. The Ga source materials were dissolved in nitrate or acetylacetonate sols, and the films prepared with acetylacetonate had a higher transmittance than those prepared with nitrate. Xu et al.[15] reported the formation of ZnO nanowires with n-type semiconductor properties on the surface of p-type delafossite, $CuGaO_2$. The multihorned composites of hexagonal $CuGaO_2$ and ZnO nanowires were successfully fabricated by a hydrothermal method. The luminescence from ZnO nanowires and electron−hole recombination at the p-n junction interface were observed in the composites.

Fig.2 Crystal structures of (a) rhombohedral (3R) $CuGaO_2$ and (b) wurtzite ZnO. (c) Projection views of 3R $CuGaO_2$ (top) and wurtzite ZnO (bottom). (d) Comparison of lattice parameters (a, b, c, α, β, and γ) between 3R $CuGaO_2$ (PDF 01-082-8561) and ZnO (PDF 04-003-2106). Cu and Zn exhibit similar stacking in the c plane, indicating the possibility to form heterostructure between them via Cu−O−Zn bonding in the c-axis direction.

Raman spectroscopy is an effective tool for nondestructive characterization of the crystal structure and lattice dynamics of various materials and can be used to obtain information on the changes in lattice vibration, lattice defects, and phase transitions.[16] For example, the half-width of a Raman peak is associated with the crystallinity;[17] a shift in the peak position indicates the strain in the crystal lattice, [18] and the covalency of bonds,[19] and the intensity of the peak reflects the physical properties such as the concentrations of components.[20] Cu-based delafossite materials are being actively studied by Raman technique,[21,22] but further investigation for them is needed because, for example, impurity phases undetectable by X-ray techniques, such as CuO[23] and Cu_2O[24], were observed, and the identification of many Raman signals that could not be assigned to those of the ideal $CuGaO_2$ structure[25] was suggested in Raman spectra of $CuGaO_2$ crystals.

To characterize the heterostructures, X-ray photoelectron (XP) spectroscopy (XPS) may provide insights into the chemical changes in the constituents of materials. Because XPS uses X-rays as the excitation source, the excitation light does not damage the material, and the charge of the insulator is easily removed. Therefore, XPS can be used to measure various materials such as polymers, metallic materials, and insulators. X-rays from Mg Kα and Al Kα sources are often used to irradiate materials. They supplement the photoelectrons emitted by the ionization of the materials so that energy analysis can be performed. When one element bonds with another, the electronic state changes and the binding energy also changes; thus, a peak shift can occur. These changes are regarded as chemical shifts and are the most important features of the XP spectra, as they enable state analysis. Gao et al.[26] recently investigated Ca-doped $CuScO_2$ through XPS and reported a possible charge balance in the $CuScO_2$ films owing to the formation of copper vacancy defects after Ca doping. A delafossite thin film on a

polymethyl methacrylate or SiO_2/Si substrate was also studied via XPS and its electrical and optical properties have been reported.[27,28]

In addition to the above-mentioned basic researches, recent works expanded the application scope of delafossite materials and heterojunctions. Especially, "self-powered solar-blind photodetectors" are one of the promising devices owing to the increasing demand for energy saving, miniaturization, and high efficiency.[29-31]

In our previous work,[10]we reported the hydrothermal synthesis of a hexagonal platelet crystal of $CuGaO_2$ with a delafossite structure and demonstrated that the particle size of $CuGaO_2$ could be controlled by adding polyethylene glycol (PEG) with different molecular weights (M_W = 6,000 and 20,000). The photocatalytic activity of $CuGaO_2/ZnO$ hybrids with a particle size of approximately 8 μm has been reported. The results showed that the hybrids had better photocatalytic properties than $CuGaO_2$ or ZnO alone, where efficient electron−hole separation in the heterojunction with a ZnO layer on the $c$plane of the delafossite crystal was identified as the driving force for the catalytic activity. In this study, powdered $CuGaO_2$ and $CuGaO_2/ZnO$ hybrids were synthesized, and Raman spectra were measured to determine theirstructures. The changes in the valence state and binding energy of the synthesized hexagonal $CuGaO_2$ and $CuGaO_2/ZnO$ hybrids were also examined by the XPS.

Experimental

Preparation of $CuGaO_2$ powder

The following reagents were used in the hydrothermal synthesis of delafossite $CuGaO_2$: $Cu(NO_3)_2 \cdot 2.5H_2O$ (Sigma-Aldrich, 99%+), $Ga(NO_3)_2 \cdot 8H_2O$ (NacalaiTesque Do.), ethylene glycol (EG) (Kishida Chem. Co.), PEG 6,000 (M_W = 6,000) (Kishida Chem. Co.), PEG 20,000 (M_W = 20,000) (Kishida Chem. Co.), and KOH (Kishida Chem. Do.). Two samples of $CuGaO_2$ were synthesized using PEG 6,000 and PEG 20,000, and the pH of the precursor solution was adjusted accordingly.

The synthesis method has been described in detail elsewhere.[10] Briefly, $Cu(NO_3)_2 \cdot 2.5H_2O$ (1 mmol) and $Ga(NO_3)_2 \cdot 8H_2O$ (1 mmol) were dissolved together in 3.6 mL of deionized water. Next, 3 mL EG and 0.1 g of PEG 6,000 or PEG 20,000 were added. KOH_{aq} (5 mmol) was introduced to each solution to adjust the pH to approximately 8.5. Each obtained deep-blue solution was poured into a Teflon-lined autoclave vessel, which was placed in an oven at 190°C.[32] After a reaction time of 56 h, the samples were naturally cooled to room temperature. A brown powder of hexagonal $CuGaO_2$ platelets was obtained. Powders containing PEG 6,000 and PEG 20,000 are denoted as CGO1 and CGO2, respectively.

Preparation of $CuGaO_2/ZnO$ hybrids

To prepare $CuGaO_2/ZnO$ samples, $Zn(CH_3COO)_2 \cdot 2H_2O$ (Kishida Chem. Co.) was used as the starting material for ZnO. As shown in **Table S1**, various quantities of $Zn(CH_3COO)_2 \cdot 2H_2O$ were added to 15 mL of

deionized water to achieve different [Zn]/[Cu] ratios. The ammonia reagent (28%, Kishida Chem. Co.) was added to adjust the pH to approximately 7, and the obtained white solution was placed in a Teflon vessel with above $CuGaO_2$ powder (CGO1 or CGO2) and annealed for 2 h at 400°C when $CuGaO_2$ remained stable. After hydrothermal treatment for 6 h in an oven at 180°C in a Teflon vessel sealed in a stainless autoclave, powdered $CuGaO_2$/ZnO samples were heated at 60°C for 2 h in air.The hybrid samples are labeled as CZ1 ([Zn]/[Cu] = 1.65 mmol/0.6 mmol = 2.75); CZ2 ([Zn]/[Cu] = 3.3 mmol/0.6 mmol = 5.5); CZ3 ([Zn]/[Cu] = 6.6 mmol/0.6 mmol = 11), which was synthesized with CGO1; and CZ4 ([Zn]/[Cu] = 9.9 mmol/0.6 mmol = 16.5), which was synthesized with CGO2. (See **Table S1** in the ESI) All of the as-synthesized CZ samples were annealed under a reducing atmosphere of H_2/N_2 (5%/95%) at 400°C for 12 h.

Characterization

The synthesized $CuGaO_2$/ZnO hybrids were examined by X-ray diffraction (XRD) analysis(PANalyticalX'pert Pro MPD) and scanning electron microscopy (SEM; JEOL, JSM-6010LA). The simulated XRD patterns of the reference crystals were obtained using the RIETAN-FP program.[33] Raman scattering experiments were conducted using an InVia Raman spectrophotometer (Renishaw). XP spectra were recorded on a PHI5000 VersaProbe X-ray photoelectron spectrometer with an Al Kα X-ray source (ULVAC-PHI).

Results And Discussion

Structural analysis of $CuGaO_2$ and $CuGaO_2$/ZnO hybrids

The structure and morphology of the interfacial $CuGaO_2$/ZnO hybrids were investigated by powder XRD and SEM. The XRD patterns of the hybridsafter H_2 annealingare shown in **Fig. 3**, along with those of the CGO1 and CGO2base crystals.[10]The simulated patterns of $CuGaO_2$ (ICDD PDF 01-082-8561 for 3R and ICDD PDF 04-011-1001 for 2H) and ZnO (ICDD PDF 04-003-2106) are also shown for comparison. As elucidated in a previous study, hydrothermal synthesis resulted in the formation of rhombohedral (3R) $CuGaO_2$ as a single phase (signified by "D" in **Fig.3**). The hydrothermal deposition of ZnOon $CuGaO_2$generated $CuGaO_2$/ZnO hybrids. As shown in **Fig.3**, New XRD peaks in CZ1−4 areattributed to wurtzite-type ZnO (indicated by the # symbol). Compared to our previous study,[10] a post-reduction process was employed here, i.e., the CZ1-4 samples were heat-treated in a hydrogen atmosphereto induce more carriers in n-type ZnO[34](see the Experimental section). For the CZ1−3 samples, where CGO1 was used as the base crystal, the X-ray reflection peaks (#) aresuperimposed on the peaks corresponding to $CuGaO_2$, and the intensity increaseswith the amount of $Zn(CH_3COO)_2 \cdot 2H_2O$ involved in the reaction (see **Table S1**).

In addition to the XRD peaks that are consistent with the results of our previous work,[10]the CZ3 sample exhibits a small peak at 30.97° (†), which indicates the formation of spinel-type cubic $CuGa_2O_4$ (*Fd-3m*) (ICDD PDF 04-001-9116).[35]There are alsothree additionalpeaks (*) in CZ3, which are not assigned to

any single component of copper oxide (Cu_2O/CuO) or gallium oxide (Ga_2O_3), but might be attributed to spinel-type tetragonal $ZnCu_2O_4$ ($I4_1/amd$).[36−38] (Fig. S2 in the ESI.) $ZnCu_2O_4$ spinel is not available in nature but has recently been revealed by computational predictions.[39-41] Its evolution might be possible during the simultaneous production of $CuGa_2O_4$, as illustrated by the reactions in **Fig.4**. Prior to the formation of $CuGaO_2$/ZnO hybrid (CZ3), $CuGaO_2$ partially decomposes in the presence of O_2 to CuO and Ga_2O_3, as shown in **Reaction 1** in **Fig.4** (confirmed by the Raman and XPS data below). According to Hautier et al.,[37] the development of $ZnCu_2O_4$ requires a more oxidizing environment. In our case, additional oxygen may be provided when water molecules adsorb on the species during the hydrothermal synthesis of ZnO. Partial formation of $ZnCu_2O_4$ and $CuGa_2O_4$ may occur in the post-reduction process (see **Reaction 2** in **Fig.4**), because the XRD patterns of the hybrids before H_2 annealing exhibited only ZnO and $CuGaO_2$ without any additional phases such as $ZnCu_2O_4$ and $CuGa_2O_4$, as shown in **Fig. S3** in the ESI. Although this is indeed a speculation, it should be considered as one of the possibilities in the reductive thermal treatment of $CuGaO_2$/ZnO hybrids with heterogeneous interfaces.

For CZ4 prepared using CGO2, the sharp (006) peak of $CuGaO_2$ is visible in the XRD pattern, and its relative intensity is high than that of (104) peak in the same crystal (I_{006}/I_{104}= 13.1, which is closer to I_{006}/I_{104} = 7.57 for CGO2 than I_{006}/I_{104} =1.57 for CGO1). It suggests the effective deposition of ZnO on the c plane (006) of the $CuGaO_2$ platelets in CZ4. (See **Fig. S4** in the ESI.)

The peaks at ~43°, ~50°, and ~61° are distinct in the XRD patterns of CZ2 and CZ3 (**Fig. 3**), but are absent in the XRD patterns of the same hybrids prior to the post-reduction process.[10] From a database survey, they were tentatively assigned to Cu_2O and metallic Cu with face-centered cubic and hexagonal structures, respectively, as shown in **Fig. S2**, and **Table S2** in the ESI. The presence of these phases is related to the [Zn]/[Cu] ratio, which will be discussed below using the SEM, Raman, and XPS data.

Figure 5 shows the SEM images of $CuGaO_2$/ZnO hybrids and $CuGaO_2$ samples. The $CuGaO_2$ base crystals exhibit well-defined and characteristic morphologies of hexagonal plates with sizes of 1−3 µm [CGO1, **Fig. 5(a)**] and 5−8 µm [CGO2, **Fig. 5(c)**]. The variations in size is related to the molecular weight of the PEG used in the synthesis.[10] For CGO2 when PEG 20,000 was used, the XRD peak corresponding to the (006) plane was relatively strong, indicating an enhanced growth of hexagonal plate-like particles. Because more −C−O−C− moieties are available in the PEG with higher molecular weight, more adsorption occurs on the (006) plane and the growth of the c plane is promoted.[10]

SEM investigation of the hybrids synthesized with various amounts of $Zn(CH_3COO)_2 \cdot 2H_2O$ has already been reported.[10] It shows that the morphological results of the samples are dependent on the starting base crystals. SEM images of the present CZ1 and CZ2 samples are given in **Fig.S5** in the ESI. In CZ1 with a nominal [Zn]/[Cu] ratio of 2.75, granular ZnO is observed on $CuGaO_2$ particles of 2 µm, while CZ2 ([Zn]/[Cu] = 5.5) shows a layer of ZnO on the surface of $CuGaO_2$ particles larger than 2 µm, and rod-shaped ZnO particles are distinct without the formation of $CuGaO_2$/ZnO hybrids. By increasing the

amount of $Zn(CH_3COO)_2 \cdot 2H_2O$, it is more likely to achieve a complete coverage of $CuGaO_2$ hexagonal plates with a ZnO layer. The SEM images of CZ3 ([Zn]/[Cu] = 11) and CZ4 ([Zn]/[Cu] = 16.5) are shown in **Fig.5(c,d)**. Unlike those in CZ1 and CZ2, the surfaces of the plate-like $CuGaO_2$ particles in CZ3 (**Fig.5(c)**) are completely covered with a ZnOlayer, and moreZnO particles are formed owing to the excess amount of $Zn(CH_3COO)_2 \cdot 2H_2O$.ForCZ4 (**Fig.5(d)**), which was hybridized with the larger CGO2 base crystal, ZnOwell covers the hexagonal $CuGaO_2$ particles to form a thick layer, and individual ZnOhexagonal blocks are also observed.The SEM-EDS results for the hybrids are shown in **Figs.S6-9** in the ESI, which reveal the presence of ZnO on the $CuGaO_2$ platelets. A comprehensive discussion related to the SEM-EDS investigation of $CuGaO_2$/ZnO hybrids was also provided in a previous work.[42]

In the last part of this session, we shall discuss on the formation mechanism of $ZnCu_2O_4$ and $CuGa_2O_4$. Firstly to be mentioned, the particle size of CGO has an important impact on the formation of $ZnCu_2O_4$ and $CuGa_2O_4$;CGO 1 and CGO2 were prepared using PEG 6,000 and PEG 20,000,respectively. Compared with CGO2, CGO1has a smaller size, indicating that it has a higher specific surface area.[42] Therefore, more oxygen molecules are likely to be adsorbed on CGO1 and more dominantly triggerthe decompositionreaction. For CZ3 when [Zn]/[Cu] ratio=11 and CGO1 is used, CuO and Ga_2O_3 produced by decomposition may react with excess ZnO to develop $ZnCu_2O_4$ and $CuGa_2O_4$ during the post-reduction process according toReactions **1 and 2**, as shown in **Fig.4**.In comparison, when [Zn]/[Cu] ratio maintains as 11 and CGO2 is used instead of CGO1, the XRD pattern (**Fig.S10** in the ESI)only shows peaks ofZnO and $CuGaO_2$, while those attributed to $ZnCu_2O_4$ and $CuGa_2O_4$are not detected. It indicates thatincreasing the particle size of $CuGaO_2$ significantly reduces the number of oxygen molecules adsorbed on the hexagonalplatelets for partial decomposition, which leads to the production of small amounts of $ZnCu_2O_4$ and $CuGa_2O_4$ phases in the subsequent reduction process and leads to more efficient hybridization with ZnO.

Micro-Raman investigation

The Raman spectra of CGO1, CGO2, CZ3, and CZ4 are shown in **Fig. 6(a)**. A Raman microscope was used for the measurement andan individual hexagonal platelet was imaged with a 100× objective. The optical pictures recorded during the spectral measurementsare shown in **Figs. 6(b)** and **6(c)**. The laser wavelength was 532 nm, and the depth of the irradiated spot was approximately 1 μm because the measurement was performed in the confocal mode (See **Figs. 6(d-f)**).[43]

As shown in **Fig. 6(a)**, Raman signals corresponding to $CuGaO_2$[25]were obtained in CGO1, CGO2, and CZ3, and a signal attributed to ZnOwasconfirmed[44]in CZ3 and CZ4.

The Raman spectra of CGO1 and CGO2 confirm the presence of $CuGaO_2$ because the peaks corresponding to the E_g, M_3, M_4, and A_{1g} modes of delafossite $CuGaO_2$crystals[25]are observed at approximately 380, 521, 610,and 780 cm^{-1}, respectively. According to the literature,[25] the modes labeled

M_3 and M_4 are attributed to the stress-induced modes of A_g (and/or B_u) and B_u at the X point, respectively, which are normally forbidden by the Raman selection rule. Our observations may be specific to the hydrothermal synthesis of $CuGaO_2$. For CGO1 and CZ3, Raman peaks with lower wavenumbers are very similar to the vibrational modes of CuO (A_g and B_g),[45] suggesting the decomposition of $CuGaO_2$, as shown in **Reaction 1** in **Fig.4**. Moreover, the observed $CuGaO_2$ peaks in the CZ3 sample shift slightly to lower wavenumbers. This shift is caused by the distortion of the $CuGaO_2$ crystal induced by strains at the heterojunction interface between $CuGaO_2$ and ZnO (see the discussion on XPS results shown later). In the Raman spectra of CZ3 and CZ4, a signal at 435 cm^{-1} is observed that was correlated to the E_2 mode of ZnO on the $CuGaO_2$ plate. In CZ4, a small peak at ~380 cm^{-1} emerged and was assigned to the A_1(TO) mode of ZnO.[44,46] These ZnO-related modes confirm that $CuGaO_2$ was successfully hybridized with ZnO. For the CZ3 sample, in addition to the ZnO peaks, signals from $CuGaO_2$ plate are also detected because ZnO layer is less than 1 µm thick (See **Fig. 6(e)**). However, CZ4 is likely to have a thicker ZnO layer because no vibrational modes of $CuGaO_2$ are visible apart from a strong ZnO peak (See **Fig. 6(f)**). Many isolated ZnO blocks appear around the hybrid because the highest $Zn(CH_3COO)_2 \cdot 2H_2O$ content was used ([Zn]/[Cu] = 16.5) in CZ4, which is in agreement with the XRD results. A comparison of the SEM images of CZ3 and CZ4 confirms that small hexagonal blocks of ZnO are formed and accumulate on the surface of the CGO2 plates in CZ4. In contrast, CZ3 has a thinner ZnO coating on the CGO1 particles. In our previous study, we found that CZ4 had better photocatalytic properties because the larger $CuGaO_2$ hexagonal plates were well-coated with ZnO.[42] A ZnO layer of sufficient thickness is expected to extract electrons from electron−hole pairs generated at the p-n interface between $CuGaO_2$ and ZnO and prevent electrons from returning to the interface with p-type $CuGaO_2$, resulting in the higher photocatalytic performance demonstrated in our previous study.

XPS results

The XP spectra of CGO2 and CZ4 are shown in **Figs. 7−10**. To measure the Cu2p and Ga2p signals in CZ4 ($CuGaO_2$ covered by ZnO), depth profiling was performed through argon ion beam sputtering. **Figures 7(a)** and **7(b)** show the Cu, Ga, O, and Zn spectra of CGO2 and CZ4 wherein and were detected at 932 and 952 eV,[47] respectively; and at 1117 and 1144 eV,[48] respectively, and at approximately 530 eV.[49] The XPS peaks of Zn were detected only for CZ4 and were assigned to and (1021.5 and 1044.5 eV, respectively). [50,51] The positions and areas of the detected XPS peaks were analyzed by deconvolution with several Gaussian and Voigt functions, which are shown in **Tables 1** and **2**.

The Cu_{2p} peak of CGO2 [approximately 932 eV in **Fig. 7(a1)**] is deconvoluted into two Voigt functions, which correspond to Cu$^+$ at 932.5 eV and Cu^{2+} at 935.8 eV, with a Cu$^+$ ratio of 76.8% and Cu^{2+} ratio of 23.2%. The Cu_{2p} peak at approximately 952 eV is also separated into Cu$^+$ and Cu^{2+} peaks at 952 and 955 eV, with ratios of 62.8% and 37.2%, respectively [**Fig. 7(a2)**]. In contrast, for the Cu_{2p} peak in the CZ4 hybrid, the peak at approximately 932 eV corresponds to 86% Cu$^+$ and 14% Cu^{2+} [**Fig. 7(b1)**], whereas the

peak at approximately 952 eV corresponds to 100% Cu$^+$ [**Fig. 7(b2)**]. For both the and peaks, the Cu$^+$ ratio clearly increases after the structural hybridization of CuGaO$_2$ with ZnO.

Table 1 Position, FWHM, and area ratio of each XPS peak for CGO2.

		Energy (eV)	FWHM (eV)	Ratio (%)	Assignment
Cu	$2p_{3/2}$	932.53	1.48	76.8	Cu(I)
		935.81	6.39	23.2	Cu(II)
	$2p_{1/2}$	952.24	1.91	62.8	Cu(I)
		954.99	5.79	37.2	Cu(II)
Ga	$2p_{3/2}$	1117.66	1.28	39.4	Ga#1
		1117.87	2.16	60.6	Ga#2
	$2p_{1/2}$	1144.59	1.23	36.5	Ga#1
		1144.78	2.04	63.5	Ga#2
O	$1s$	530.29	1.31	69.3	O#1
		531.73	1.86	30.7	O#2

Table 2 Position, FWHM, and area ratio of each XPS peak for CZ4.

		Energy (eV)	FWHM (eV)	Ratio (%)	Assignment
Cu	$2p_{3/2}$	932.69	2.45	86.0	Cu(I)
		935.67	6.08	14.0	Cu(II)
	$2p_{1/2}$	952.69	2.51	100.0	Cu(I)
		-	-	-	Cu(II)
Ga	$2p_{3/2}$	1117.78	2.40	95.5	Ga#3
		1117.97	0.69	4.5	Ga#4
	$2p_{1/2}$	1144.74	2.16	97.0	Ga#3
		1145.06	0.35	3.0	Ga#4
Zn	$2p_{3/2}$	1021.46	1.28	25.3	Zn#1
		1021.82	2.17	74.7	Zn#2
	$2p_{1/2}$	1044.59	1.38	37.3	Zn#1
		1044.99	2.22	62.7	Zn#2
O	$1s$	530.28	1.16	33.1	O#1
		531.16	2.70	66.9	O#2

Regarding Ga content, the Ga$_{2p}$ peak at 1117 eV is deconvoluted into two Gaussian functions. For CGO2, Ga#1 at 1117.7 eV accounts for 39.4%, and Ga#2 at 1117.9 eV accounts for 60.6%. The former has a narrow full width at half maximum (FWHM) of ~1.3 eV, and the latter has a broader FWHM of ~2.2 eV. It is noted that the central positions are almost the same despite of the difference in the FWHM, as shown in **Figs. 8(a1)** and **8(a2)**. A comparison of the binding energies of metallic Ga (1116 eV)[52] and Ga$_2$O$_3$ (1118 eV)[48] reveals that the observed XPS peak cannot be attributed to the lower valence state of Ga. Thus, Ga has to be in a trivalent state and be coordinated with oxygen. For the Ga$_{2p}$ peak at a lower energy of approximately 1144 eV, the Ga#1 peak at 1144.6 eV, with a FWHM of ~1.2 eV, is found to account for 36.5%, and the Ga#2 peak at 1144.8 eV, with a FWHM of ~2.0 eV, account for 63.5%; all of the peak tops fall within a

0.2 eV binding energy range. As shown in **Figs. 8(b1)** and **8(b2)**, the XPS signal of the hybrid sample is smaller because of the formation of the ZnO layer on CuGaO$_2$. However, a meaningful deconvolution analysis can be performed. Interestingly, the analysis of the Ga$_{2p}$ peak of the hybrid shows that the ratio of the broader component with a FWHM of 2.2–2.4 eV (denoted as Ga#3) significantly increases (by

more than 95%) for both and , which appear at 1117.8 and 1144.7 eV, respectively. These peakshave almost the same values as the Ga#2 peak in CGO2. The narrower component (Ga#4) shows a peak at 1118.0 eV for and 1145.1 eV for which are at a higher energy side than the corresponding narrower component of CGO2 (Ga#1), possibly indicating the effect of the formation of the $CuGaO_2$/ZnO hybrid. Because the peak difference between the deconvoluted Gaussian functions is within 0.2 eV in both cases, the XPS signals can be expressed by a single Gaussian function with an FWHM of 2.2–2.4 eV. These results indicate that the $CuGaO_2$ base crystal CGO2 had well-formed GaO_6 octahedra on the inner side (for Ga#1) and GaO_6 octahedra with a relatively disordered chemical bonding state near the surface (for Ga#2). In addition, sufficient ZnO coverage of $CuGaO_2$ weakened the XPS signal, but the detected signal was sensitive to GaO_6 octahedra near the heterojunction with ZnO; consequently, the Ga#3 peak of the hybrid has a larger FWHM.

Regarding the oxygen (**Fig. 9**), the O_{1s} peak is deconvoluted into two Gaussian peaks, O#1 (530.3 eV) and O#2 (531.7 eV), and the O_{1s}peaks in $CuGaO_2$[**Fig. 9(a)**] are 69.3% O#1 and 30.7% O#2. For the CZ4 hybrid [**Fig. 9(b)**], however, the O_{1s} is 33.1% O#1 at 530.3 eV and 66.9% O#2 at 531.2 eV. According to the literature, adsorbed H_2O molecules and OH moieties are related to XPS peaks at 532.8 and 531.7 eV, respectively.[49] Thus, the O#2 signals for CGO2 and CZ4 are attributed to OH moieties, and the observed binding energies for O#1 in these samples are originated from O in the $CuGaO_2$ and ZnO structures, respectively.The ratio of O#2 increased from 30.7% in CGO2 to 66.9% in CZ4, which is attributed to the H_2 post-annealing, subsequently leading to an increase in the OH content.

Zn XPS signals were observed only for CZ4. As shown in **Fig. 10**, the peak at 1021.5 eV [**Fig. 10(a1)**] is deconvoluted into two Voigt functions, i.e., Zn#1 at 1021.5 eV accounts for 25.3% and Zn#2 at 1021.8 eV accounts for 74.7%. The peak at approximately 1044.6 eV [**Fig. 10(a2)**] is deconvoluted into Zn#1 at 1044.6 eV (37.3%) and Zn#2 at 1045 eV (62.7%); this result indicates that Zn is in the +2 oxidation state[51,52] which corresponds to the formation of ZnO crystals.

To summarize, the $CuGaO_2$/ZnOhybridis formed with a ZnO layer on the $CuGaO_2$ particles; thus, the surface state is significantly different from that of the $CuGaO_2$ base crystal. The (006) plane of $CuGaO_2$ is completely covered with the ZnO layer, in which oxygen has four-fold coordination with Zn (OZn_4), whereas in $CuGaO_2$, oxygen is four-fold-coordinated with Cu and three Ga atoms combined with the GaO_6 octahedron, that is, an $OCuGa_3$ tetrahedron is present [**Figs. S1(a)** and **S11** in the ESI]. The O 1s detected in XPS can potentially indicate the changing environment of the constituent oxygen atoms in ZnO and $CuGaO_2$. However, this peak is too broad for a detailed separation of the contributions.

Conclusions

The heterojunction between delafossite $CuGaO_2$ and wurtzite ZnO was investigated using $CuGaO_2$/ZnO hybrids synthesized via a hydrothermal method. XRD and SEM investigations of the hybrids confirmed the successfuldeposition of ZnO on $CuGaO_2$, and the subsequent reduction processinducedadditional

reactionsbetween $CuGaO_2$ and ZnO, which could be tuned by varying the particle size of $CuGaO_2$ and [Zn]/[Cu] ratio. Micro-Raman observations confirmed the vibrational modes of ZnO in the $CuGaO_2$/ZnO hybrids. XPS profiles showed the presence of Cu, Ga, and O in the $CuGaO_2$ and $CuGaO_2$/ZnO hybrids, and quantitative analysis of two types of Cu (Cu^+ and Cu^{2+}) was performed. The Cu^+ ratio was higher in the hybrids than in the $CuGaO_2$ crystal. The Ga XP spectra indicated more distortions on the surface than in the inner structure of the $CuGaO_2$ base crystal and more strains were involved at the heterojunction interface between $CuGaO_2$ and ZnO. The formation of hybrids of $CuGaO_2$ and ZnOwas found to be accompanied by an increase in the Cu^+ and OH contents after H_2 post-annealing, which could be responsible for the effective carrier separation observed in the heterojunction.

Declarations

Author Contributions

Minuk Choi: investigation, writing the original draft, data curation, and visualization. Christoph Brabec: supervisor, project administration.TomokatsuHayakawa: conceptualization, methodology, resources, data curation, visualization, supervision, validation, writing-review and editing, and project administration.

Conflicts of interest

There are no conflicts to declare.

Data availability

The datasets used and/or analysed during the current study available from the corresponding author on reasonable request.

References

[1] X. Chen, S. Shen, L. Guo and S. S. Mao, "Semiconductor-based photocatalytic hydrogen generation", *Chem. Rev.*, 2010, **110**(11), 6503–6570.

[2] A. Mills, R. H. Davies and D. Worsley, "Water purification by semiconductor photocatalysis", *Chem. Soc. Rev.*, 1993, **22**, 417–425.

[3] M. Yu, G. Natu, Z. Ji and Y. Wu, "p-Type dye-sensitized solar cells based on delafossite $CuGaO_2$ nanoplates with saturation photovoltages exceeding 460 mV", *J. Phys. Chem. Lett.*, 2012, **3**(9), 1074–1078.

[4] J. Li, W. Fang, C. Yu, W. Zhou, L. Zhu and Y. Xie, "Ag-based semiconductor photocatalysts in environmental purification," *Appl. Surf. Sci.*, 2015, **358**, Part A, 46–56.

[5] J. Ke, M. A. Younis, Y. Kong, H. Zhou, J. Liu, L. Lei and Y. Hou, "Nanostructured ternary metal tungstate-based photocatalysts for environmental purification and solar water splitting: A review", *Nano-Micro Lett.*, 2018, **10**, 69.

[6] Z. Zhang and J. T. Yates. Jr., "Band bending in semiconductors: Chemical and physical consequences at surfaces and interfaces", *Chem. Rev.*, 2012, **112**(10), 5520–5551.

[7] M. Pirhashemi, A. Habibi-Yangjeh and S. R. Pouran, "Review on the criteria anticipated for the fabrication of highly efficient ZnO-based visible-light-driven photocatalysts", *J. Ind. Eng. Chem.*, 2018, **62**, 1–25.

[8] S. Dong, J. Feng, M. Fan, Y. Pi, L. Hu, X. Han, M. Liu, J. Sun and J. Sun, "Recent developments in heterogeneous photocatalytic water treatment using visible light responsive photocatalysts: a review", *RSC Adv.*, 2015, **5**, 14610.

[9] R. D. Zhao, Y. M. Zhang, Q. L. Liu and Z. Y. Zhao, "Effects of the preparation process on the photocatalytic performance of delafossite $CuCrO_2$", *Inorg. Chem.*, 2020, **59**(22), 16679–16689.

[10] M.U. Choi and T. Hayakawa, "Hydrothermal synthesis and photocatalytic properties of $CuGaO_2$/ZnO hexagonal platelet hybrids", *Mater. Res. Bull.*, 2019, **113**, 84–89.

[11] J. Wang, V. Ibarra, D. Barrera, L. Xu, Y. J. Lee and J. W. P. Hsu, "Solution synthesized p-type copper gallium oxide nanoplates as hole transport layer for organic photovoltaic devices", *J. Phys. Chem. Lett.*, 2015, **6**, 1071–1075.

[12] I. Suzuki, H. Nagatani, M. Kita, Y. Iguchi, C. Sato, H. Yanagi, N. Ohashi and T. Omata, "First-principles study of $CuGaO_2$ polymorphs: Delafossiteα-$CuGaO_2$ and wurtzite β-$CuGaO_2$", *Inorg. Chem.*, 2016, **55**, 7610–7616.

[13] Z. Xu, D. Xiong, H. Wang, W. Zhang, X. Zeng, L. Ming, W. Chen, X. Xu, J. Cui, M. Wang, S. Powar, U. Bach and Y. Cheng, "Remarkable photocurrent of p-type dye-sensitized solar cell achieved by size controlled $CuGaO_2$ nanoplates", *J. Mater. Chem. A*, 2014,**2**, 2968–2976.

[14] T. Ehara, "Preparation of $CuGaO_2$ thin film by a sol-gel method using two kinds of metal source combination", *J. Mater. Sci. Chem. Eng.*, 2018, **6**, 68–78.

[15] Y. Xu, G. Ma, G. Wang, L. Shi, H. Zhang, L. Jin, X. Ma, Y. Zou, J. Yin and Y. Li, "Interface state luminescence and sub-bandgap absorption based on $CuGaO_2$ nanoplates/ZnO nanowires heterostructure arrays", *Phys. Status Solidi B*, 2018, **255**, 1800391.

[16] M. Han, Y. Lu, Y. Liu, Z. Hu, G. Chen, K. Jiang, J. Zhang and W. Li, "Raman scattering measurements of phonon anharmonicity in the delafossite $CuGa_{1-x}Cr_xO_2$ ($0 \leq x \leq 1$) films", *J. Raman Spectrosc.*, 2020, **51**, 851−859.

[17] H. Wang, C. K. Mann and T. J. Vickers, "Effect of powder properties on the intensity of Raman scattering by crystalline solids", *Appl. Spectrosc.,* 2002, **56**(12), 1538−1544.

[18] S. Wirths, A. T. Tiedemann, Z. Ikonic, P. Harrison, B. Holländer, T. Stoica, G. Mussler, M. Myronov, J. M. Hartmann, D. Grützmacher, D. Buca and S. Mantl, "Band engineering and growth of tensile strained Ge/(Si) GeSn heterostructures for tunnel field effect transistors", *Appl. Phys. Lett.,* 2013, **102**(19), 192103.

[19] L. Laurentius, S. R. Stoyanov, S. Gusarov, A. Kovalenko, R. Du, G. P. Lopinski and M. T. McDermott, "Diazonium-derived aryl films on gold nanoparticles: Evidence for a carbon-gold covalent bond", *ACS Nano,* 2011, **5**, 4219−4227.

[20] J. Bood, C. Brackmann, P.-E. Bengtsson and M. Aldén, "Multipoint temperature and oxygen-concentration measurements using rotational coherent anti-Stokes Raman spectroscopy", *Opt. Lett.,* 2000, **25**, 1535−1537.

[21] M. J. Han, K. Jiang, J. Z. Zhang, Y. W. Li, Z. G. Hu and J. H. Chu, "Temperature dependent phonon evolutions and optical properties of highly c-axis oriented $CuGaO_2$ semiconductor films grown by the sol-gel method", *Appl. Phys. Lett.,* 2011, **99**, 131104.

[22] J. Ahmed and Y. Mao, "Synthesis, characterization and electrocatalytic properties of Delafossite $CuGaO_2$", *J. Solid State Chem.,* 2016, **242**(1), 77−85.

[23] L. Debbichi, M. C. Marco de Lucas, J. F. Pierson and P. Krüger, "Vibrational properties of CuO and Cu_4O_3 from first-principles calculations, and Raman and infrared spectroscopy", *J. Phys. Chem. C*, 2012, **116**(18), 10232−10237.

[24] G. Prabhakaran and R. Murugan, "Room temperature ferromagnetic properties of Cu_2O microcrystals", *J. Alloys Compd.,* 2013, **579**, 572−575.

[25] J. Pellicer-Porres, A. Segura, E. Martínez, A. M. Saitta, A. Polian, J. C. Chervin and B. Canny, "Vibrational properties of delafossite $CuGaO_2$ at ambient and high pressures", *Phys. Rev. B,* 2005, **72**, 064301.

[26] H. Gao, X. Zeng, Q. Guo, Z. Yang, Y. Deng, H. Li and D. Xiong, "P-type transparent conducting characteristics of delafossite Ca doped $CuScO_2$ prepared by hydrothermal synthesis", *Dalton Trans.,* 2021, **50**, 5262−5268.

[27] C-Y. Chen, S. Sakthinathan, C-L. Yu, C-C. Wang, T-W. Chiu and Q. Han, "Preparation and characterization of delafossite $CuCrO_2$ film on flexible substrate", *Ceram. Int.,* 2021, **47**, 23234−23239.

[28]S. Li, X. Zhang, P. Zhang, X. Sun, H. Zheng and W. Zhang, "Preparation and characterization of solution-processed nanocrystalline p-Type $CuAlO_2$ thin-film transistors", *Nanoscale Res. Lett.,* 2018, **13**(1), 259.

[29] C. Wu, L. Qiu, S. Li, D. Guo, P. Li, S. Wang, P. Du, Z. Chen, A. Liu, X. Wang, H. Wu, F. Wu, W. Tang, "High Sensitive and Stable Solution-Processed All Inorganic Self-powered Solar-blind Photodetector based on $CuMO_2/Ga_2O_3$ p-n heterojunction", *Mater. Today Phys.*, 2021, **17**, 100335.

[30] C. He, D. Guo, K. Chen, S. Wang, J. Shen, N. Zhao, A. Liu, Y. Zheng, P. Li, Z. Wu, C. Li, F. Wu, W. Tang, "α-Ga_2O_3 Nanorod Array−Cu_2O Microsphere p−n Junctions for Self-Powered Spectrum-Distinguishable Photodetectors", *ACS Appl. Nano Mater.,* 2019, **2**(7), 4095-4103.

[31] D. Guo, K. Chen, S. Wang, F. Wu, A. Liu, C. Li, P. Li, C. Tan, W. Tang, "Self-Powered Solar-Blind Photodetectors Based on α/β Phase Junction of Ga_2O_3", *Phys. Rev. Applied.*, 2020, **13**, 024051.

[32] R. Srinivasan, B. Chavillon, C. Doussier-Brochard, L. Cario, M. Paris, E. Gautron, P. Deniard, F. Odobel and S. Jobic, Tuning the size and color of the p-type wide band gap delafossite semiconductor $CuGaO_2$ with ethylene glycol assisted hydrothermal synthesis, *J. Mater. Chem.,* 2008, **18**, 5647−5653.

[33]F. Izumi and K. Momma, "Three-dimensional visualization in powder diffraction", *Solid State Phenom.,* 2007, **130**, 15−20.

[34] J. Huang, U. R. Krishna, M. Lemberger, M. P. M. Jank, H. Ryssel and L. Frey, "Impact of forming gas annealing on ZnO-TFTs," 2010 10th IEEE International Conference on Solid-State and Integrated Circuit Technology, 2010, 1548-1550.

[35] D. Gingasu, I. Mindru, L. Patron, G. Marinescu, F. Tuna, S. Preda, J. M. Calderon-Moreno and C. Andronescu, "Synthesis of $CuGa_2O_4$ nanoparticles by precursor and self-propagating combustion method", *Ceram. Int.,* 2012, **38**, 6739−6751.

[36] Materials Project: mp-1541943. https://materialsproject.org/materials/mp-1541943/ (last accessed: September 22, 2021).

[37] G. Hautier, C. C. Fischer, A. Jain, T. Mueller and G. Ceder, "Finding nature's missing ternary oxide compounds using machine learning and density functional theory", *Chem. Mater.,* 2010, **22**, 3762−3767.

[38] D.O. Samson and E. K. Makama,"Effect of Concentration on Morphological, Optical and Electrical Properties of Copper Doped Zinc Oxide Thin Films Deposited by Electrostatic Spray Pyrolysis (ESP) Technique", *J. Mater. Sci. Res. Rev.*2018, **1**(4),1-14.

[39] M. Stoica, A. Faghaninia, X. Sun and C. S. Lo, "Computational design of p-type transparent conductors for photovoltaic applications", Proceedings of IEEE 40th Conference on Photovoltaic Specialists (PVSC) (2014) 260−265. DOI:10.1109/PVSC.2014.6924882.

[40] M. Stoica and C. S. Lo, "P-type Zinc Oxide Spinels: Application to TransparentConductors and Spintronics", *New J. Phys.* 2014, **16**, 055011.

[41] N.R. Singstock, C.J. Bartel, A.M. Holder, C.B. Musgrave, "High-Throughput Analysis of Materials for Chemical Looping Processes", *Adv.Energy Mater.*2020, **10**, 2000685.

[42] M. Choi, S. Yagi, Y. Ohta, K. Kido and T. Hayakawa, "Estimation of delafossite p-type $CuGaO_2$/ZnO hybrids as semiconductor photocatalyst by controlling particle size", *J. Phys. Chem. Solids,* 2021, **150**, 109845.

[43] G. Shu, B. Dai, V. G. Ralchenko, A. A. Khomich, E. E. Ashkinazi, A. P. Bolshakov, S. N. Bokova-Sirosh, K. Liu, J. Zhao, J. Han and J. Zhu, "Epitaxial growth of mosaic diamond: Mapping of stress and defects in crystal junction with a confocal Raman spectroscopy", *J. Cryst. Growth,* 2017, **463**, 19−26.

[44] F. Decremps, J. Pellicer-Porres, A. M. Saitta, J. C. Chervin and A. Polian, "High-pressure Raman spectroscopy study of wurtzite ZnO", *Phys. Rev. B*, 2002, **65**, 092101.

[45] A. P. Litvinchuk, A. Möller, L. Debbichi, P. Krüger, M. N. Lliev and M. M. Gospodinov, "Second-ordeRaman scattering in CuO", *J. Phys.: Condens. Matter,* 2013, **25**, 105402.

[46] R. Cuscó, E. Alarcón-Lladó, J. Ibáñez, L. Artús, J. Jiménez, B. Wang and M. J. Callahan, "Temperature dependence of Raman scattering in ZnO", *Phys. Rev.B*, 2007, **75**, 165202.

[47] L. Makhova, D. Wett, M. Lorenz and I. Konovalov, "X-ray spectroscopic investigation of forbidden direct transitions in $CuGaO_2$ and $CuInO_2$", *Phys. Status Solidi*, 2006, **11**, 2861−2866.

[48] C. V. Ramana, E. J. Rubio, C. D. Barraza, A. Miranda Gallardo, S. McPeak, S. Kotru and J. T. Grant, "Chemical bonding, optical constants, and electrical resistivity of sputter-deposited gallium oxide thin films", *J. Appl. Phys.,* 2014, **115**, 043508.

[49] J. T. Kloprogge and B. J. Wood, "Systematic XPS study of gallium-substituted boehmite", *J. Mater. Sci.,* 2016, **51**, 5436−5444.

[50] M. Salavati-Niasari, F. Davar and A. Khansari, "Nanosphericals and nanobundles of ZnO: Synthesis and characterization", *J. Alloys Compds.,* 2011, **509**, 61−65.

[51] R. Al-Gaashani, S. Radiman, A. R. Daud, N. Tabet and Y. Al-Douri, "XPS and optical studies of different morphologies of ZnO nanostructures prepared by microwave methods", *Ceram. Int.,* 2013, **39**, 2283−2292.

[52] G. Schön, "Auger and direct electron spectra in X-ray photoelectron studies of zinc, zinc oxide, gallium and gallium oxide", *J. Electron Spectrosc. Relat. Phenom.,* 1973, **2**, 75−86.
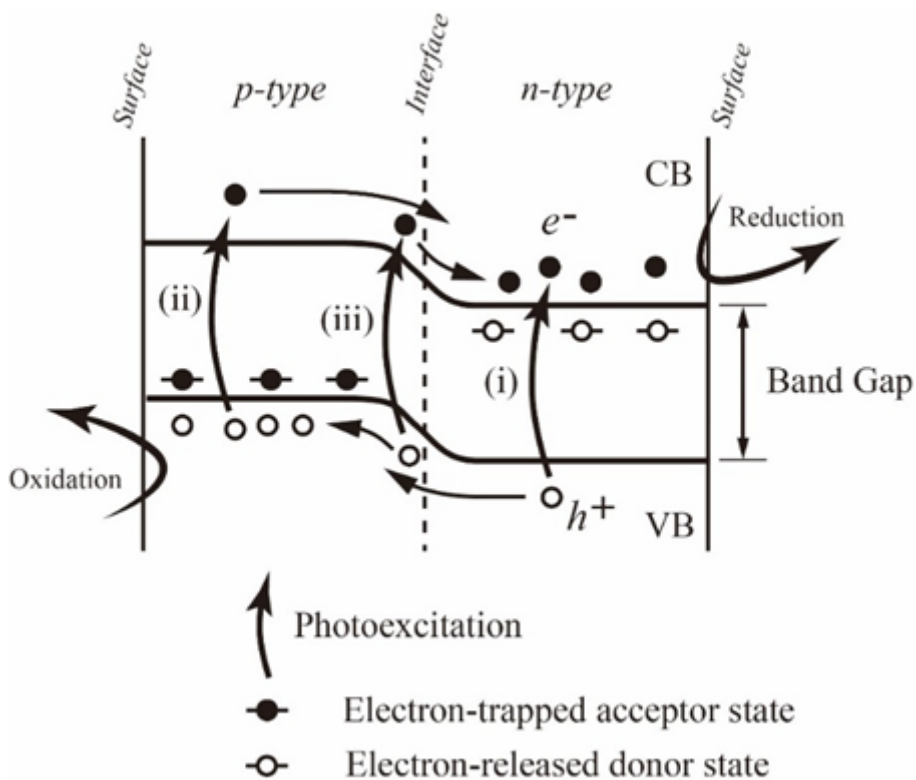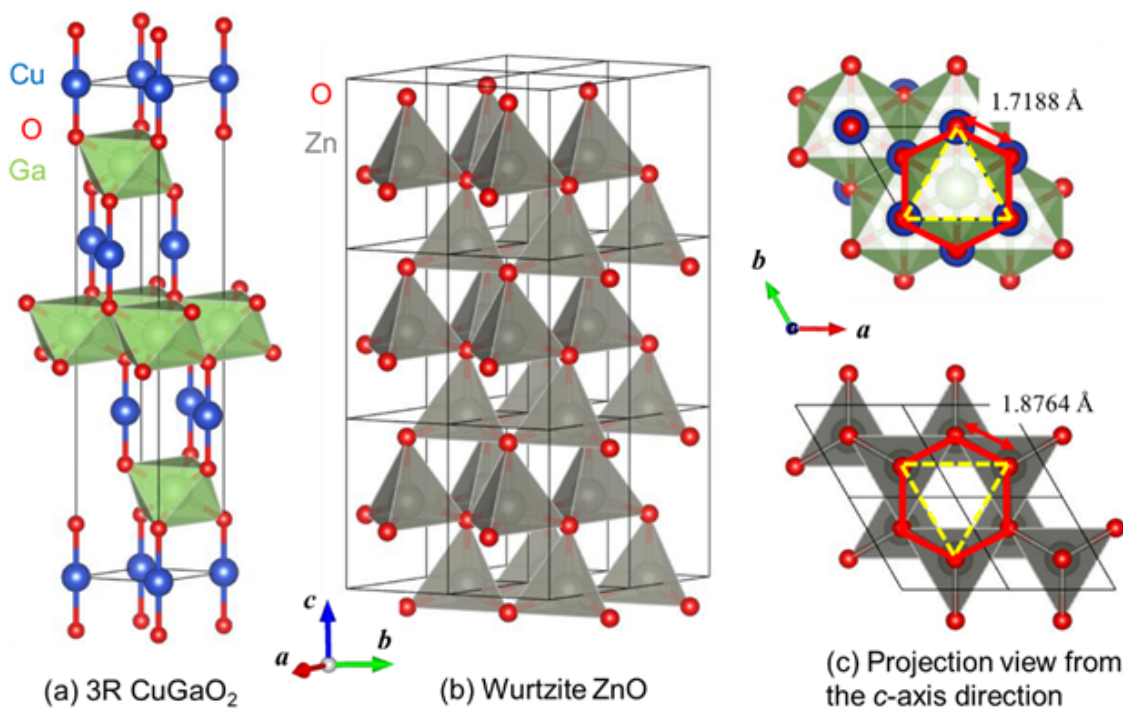
Figures

Figure 1

Schematic illustration of photocatalysis mechanism of a heterostructure using p- and n-type semiconductors under light illumination above band-gap energy. Potential slope at the interface between p- and n-type semiconductors can effectively separate generated electron−hole($e^-−h^+$) pairs.[7,8] VB: valence band, CB, conduction band. (See the main text about (i)-(iii)).

	CuGaO$_2$	ZnO
a / Å	2.9770	3.2501
b / Å	2.9770	3.2501
c / Å	17.171	5.207
α / °	90	90
β / °	90	90
γ / °	120	120

(d) Lattice parameters of 3R CuGaO$_2$ and ZnO

(a) 3R CuGaO$_2$

(b) Wurtzite ZnO

(c) Projection view from the c-axis direction

Figure 2

Crystal structures of (a) rhombohedral (3R) $CuGaO_2$ and (b) wurtzite ZnO. (c) Projection views of 3R $CuGaO_2$(top) and wurtzite ZnO (bottom). (d) Comparison of lattice parameters (*a*, *b*, *c*, *α*, *β*, and *γ*) between 3R $CuGaO_2$ (PDF 01-082-8561) and ZnO (PDF 04-003-2106). Cu and Zn exhibit very similar stacking in the *c* plane, indicating the possibility to form heterostructure between them via Cu−O−Zn bonding in the *c*-axis direction.
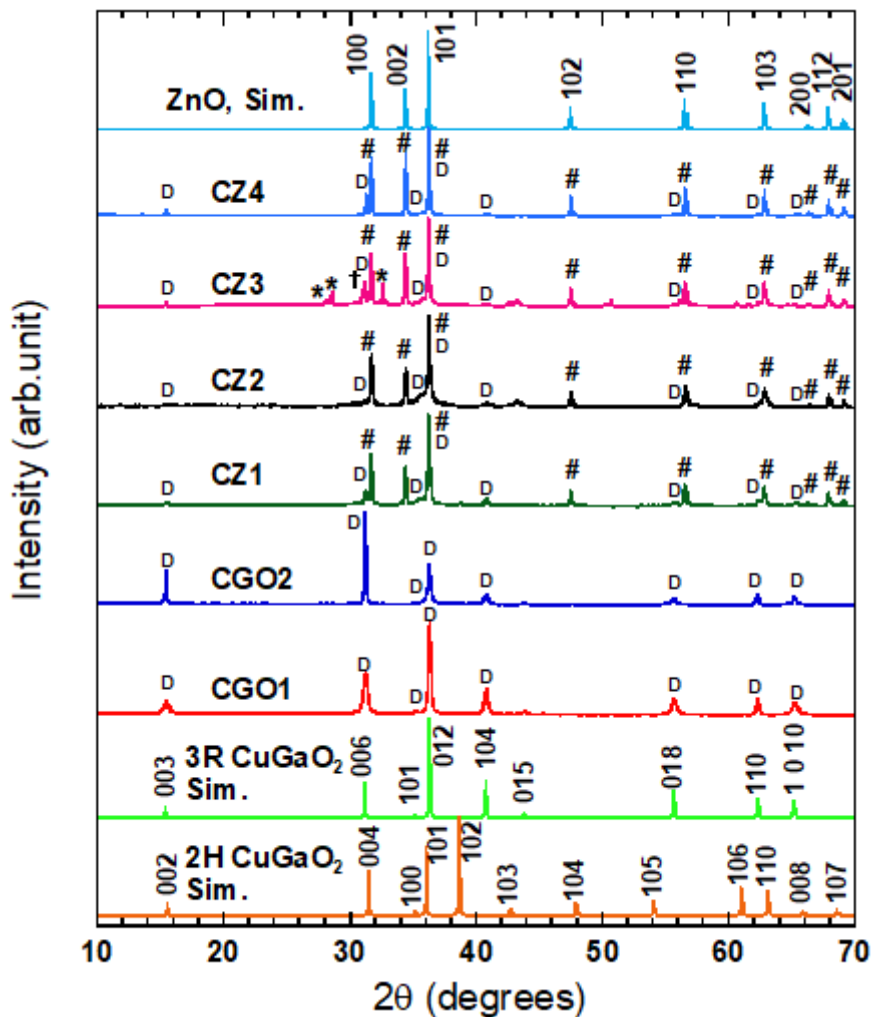

Figure 3

XRD patterns of the $CuGaO_2$/ZnO hybrid samples post-annealed in H_2, together with those of the $CuGaO_2$ base crystals (CGO1 and CGO2) for comparison.[10] The simulated patterns of 3R and 2H$CuGaO_2$ and ZnO are also shown. The symbols D, #, †, and * indicate 3R$CuGaO_2$, ZnO, $CuGa_2O_4$, and $ZnCu_2O_4$, respectively. (See the main text for details.)

$$4CuGaO_2 + O_2 \rightarrow 4CuO + 2Ga_2O_3 \qquad \textbf{(Reaction 1)}$$

$$4CuGaO_2 + 4CuO + 2Ga_2O_3 + 2ZnO + 4H_2O \underset{+H_2}{\rightarrow} 2ZnCu_2O_4 + 4CuGa_2O_4 + 4H_2 \uparrow \qquad \textbf{(Reaction 2)}$$
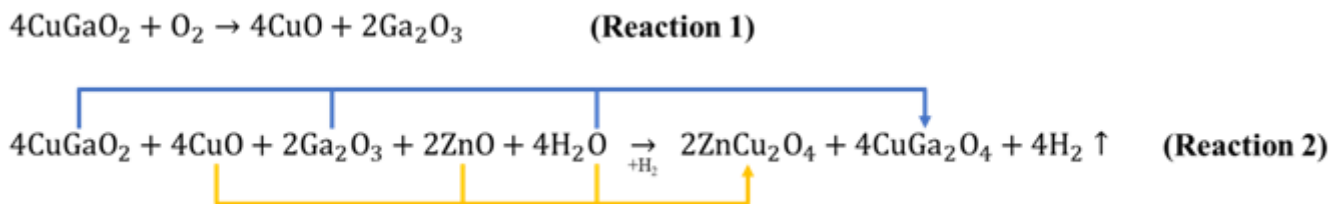
Figure 4

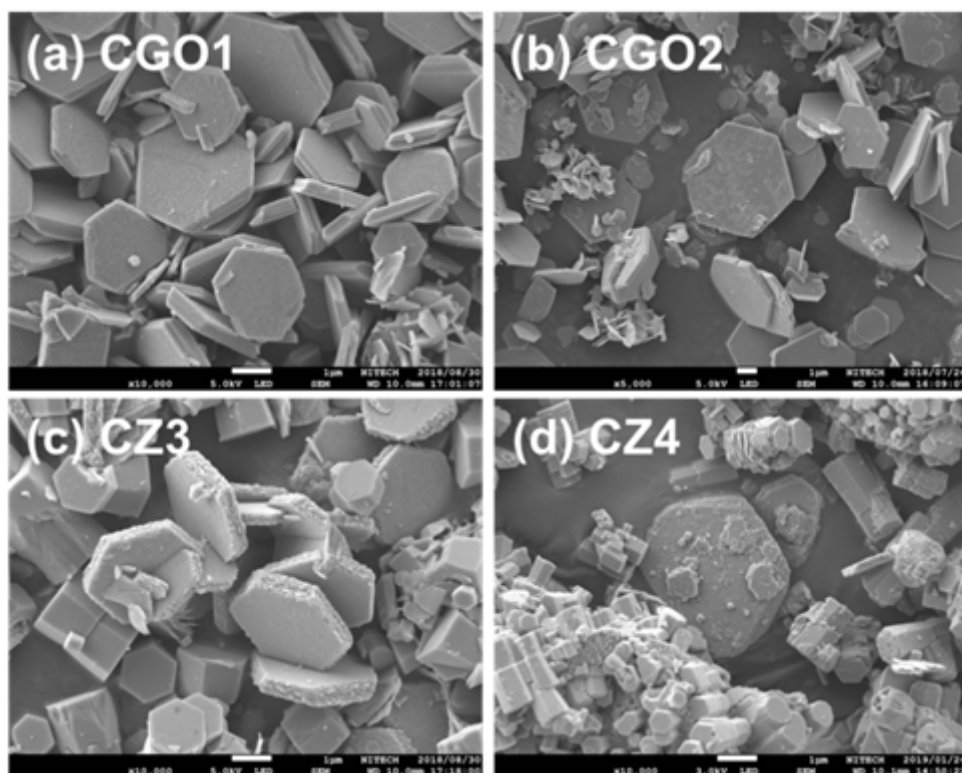Reactions for possible formations of $ZnCu_2O_4$ and $CuGa_2O_4$.

Figure 5

SEM images of the $CuGaO_2$ base crystals (a, b) and $CuGaO_2$/ZnO hybrids (c, d). CGO1 (a) was synthesized with PEG6,000 while CGO2 (b) with PEG20,000. CZ3 (c) and CZ4 (d) were hybridized with CGO1 and COG2, respectively. The scale bar shows 1 µm. [Zn]/[Cu] ratio was adjusted for CZ3 and CZ4, as given in **Table S1** in the ESI. (See the details in Experimental section). SEM images of the CZ1 and CZ2 samples can be found in **Fig. S5** in the ESI.
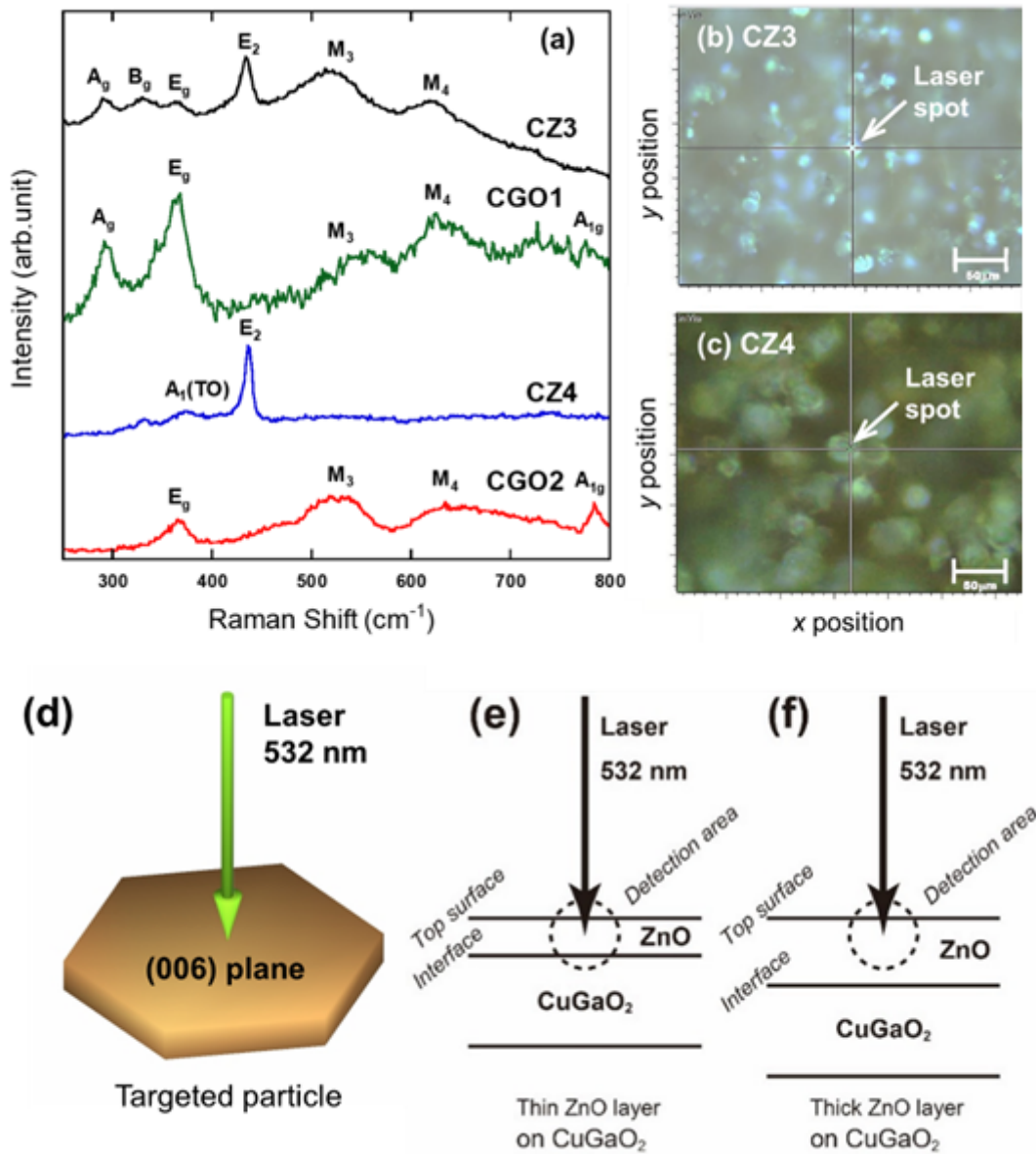
Figure 6

(a) Raman spectra of $CuGaO_2$ and $CuGaO_2/ZnO$, and optical microscopy images of (b) CZ3 and (c) CZ4. The scale bar is 50 μm. (d) Illustration of micro-Raman experiment and (e,f) schematical drawings of depth region for the confocal Raman detection.
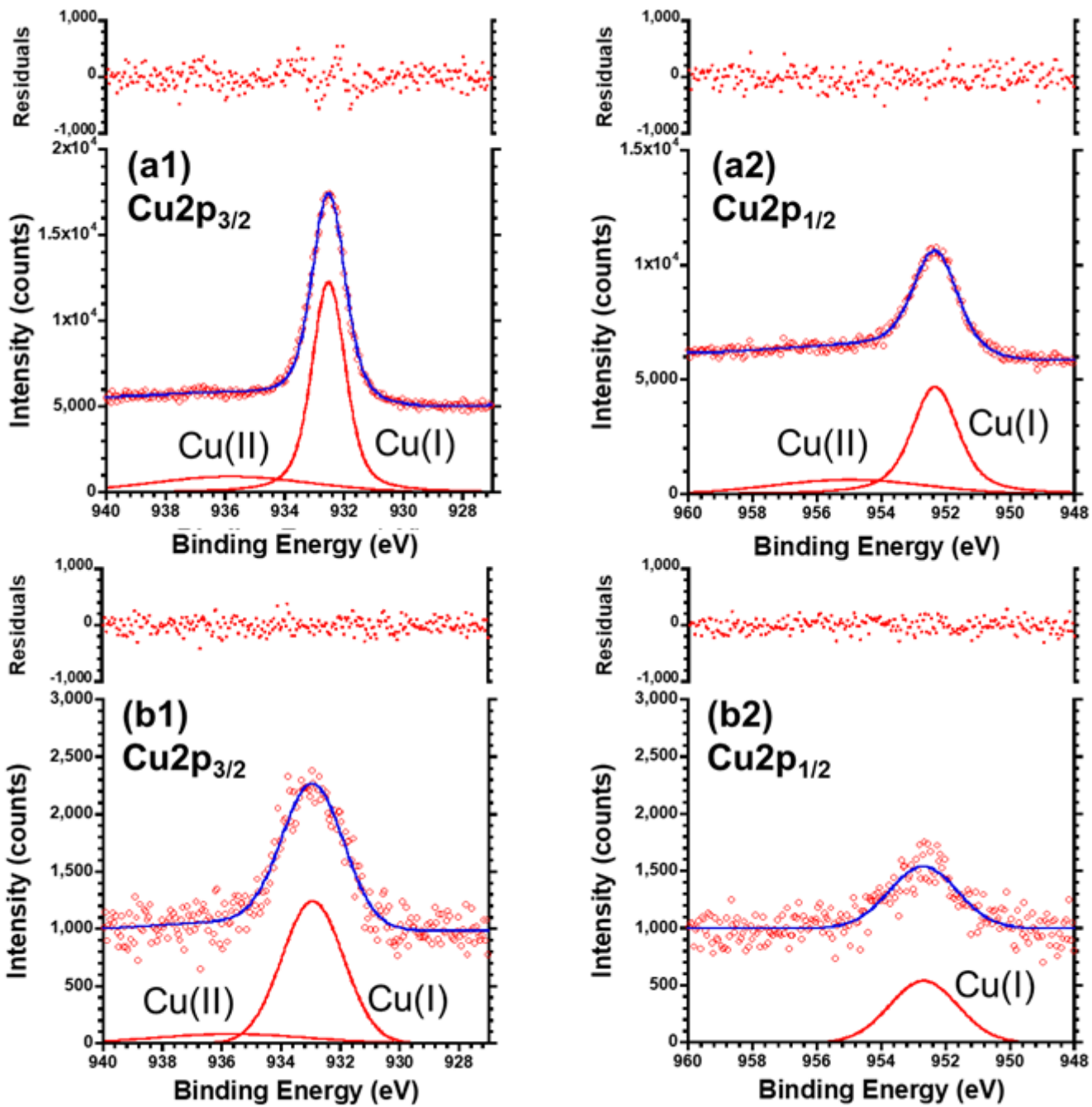
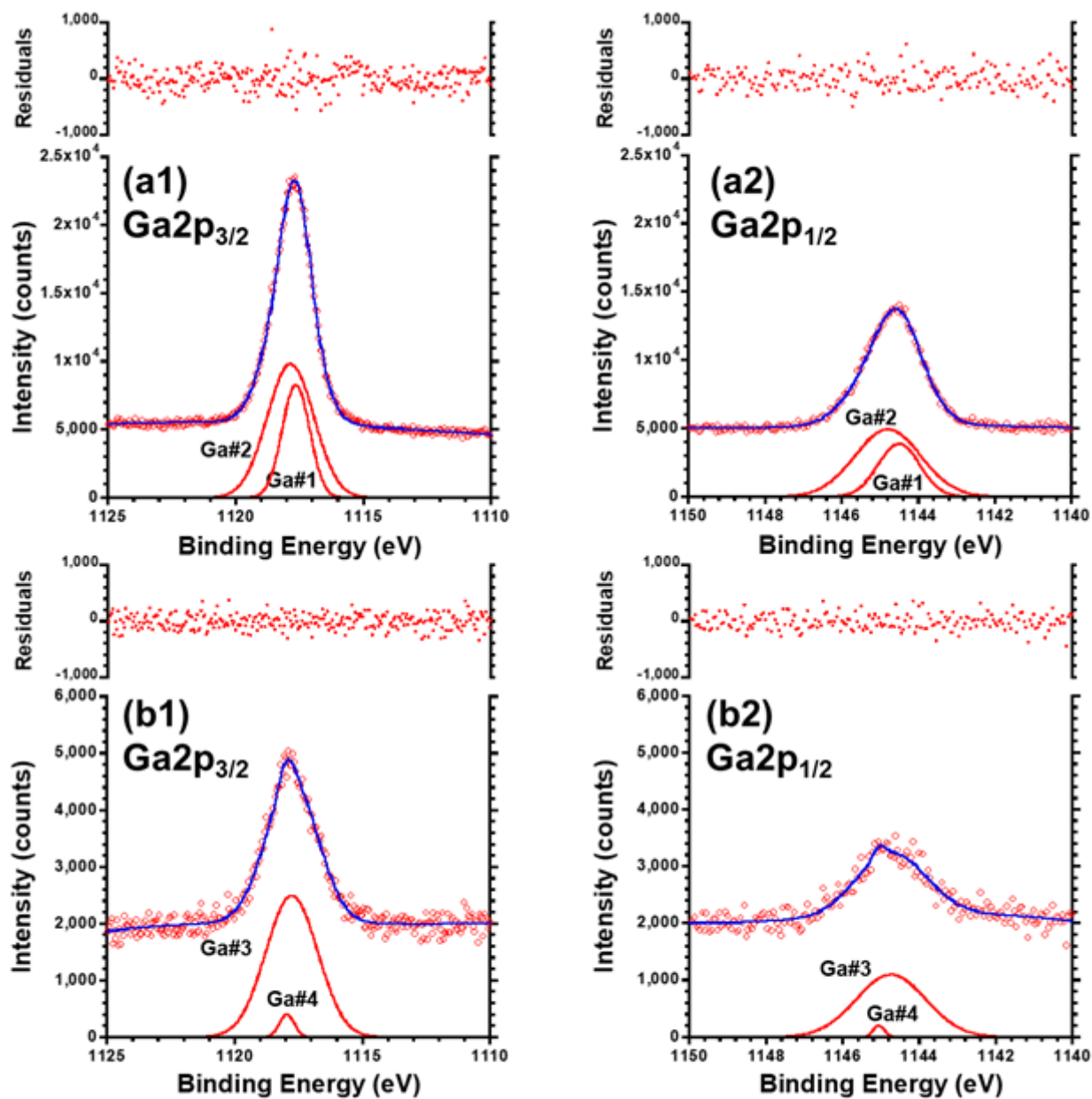Figure 7

Cu 2p XP spectra of (a1,2) CGO2 and (b1,2) CZ4.

Figure 8

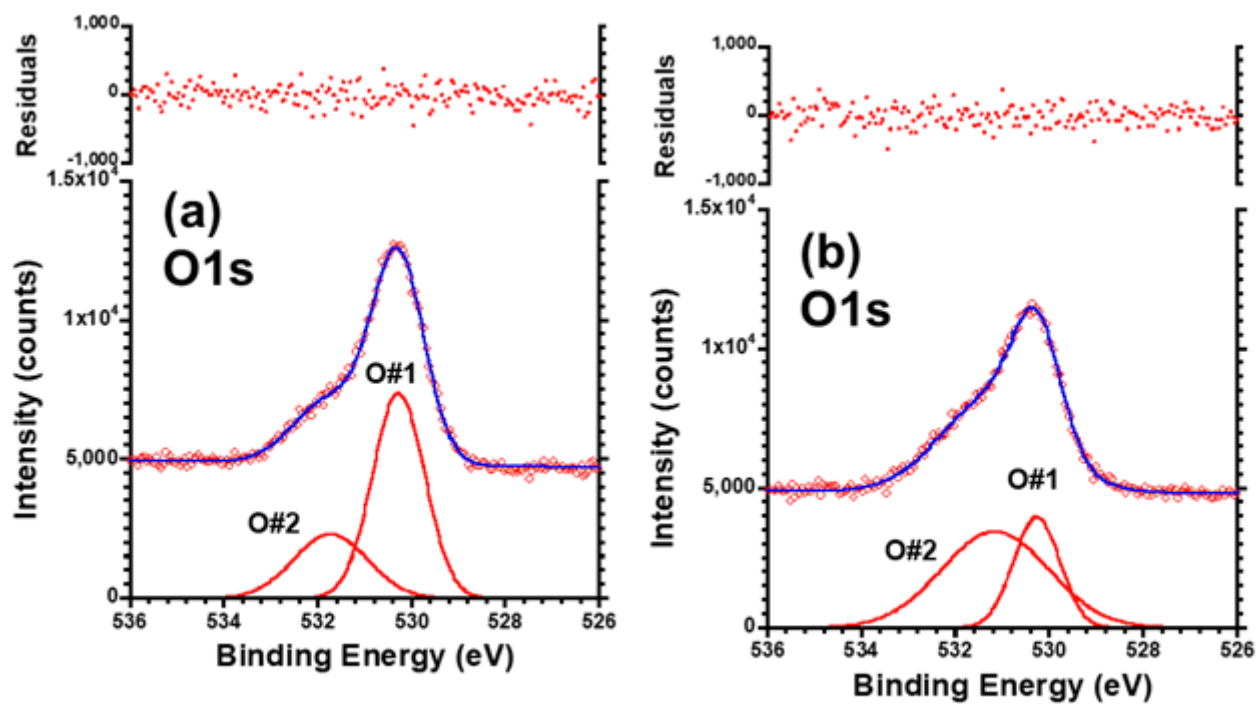Ga 2p XP spectra of (a1,2) CGO2 and (b1,2) CZ4.

Figure 9

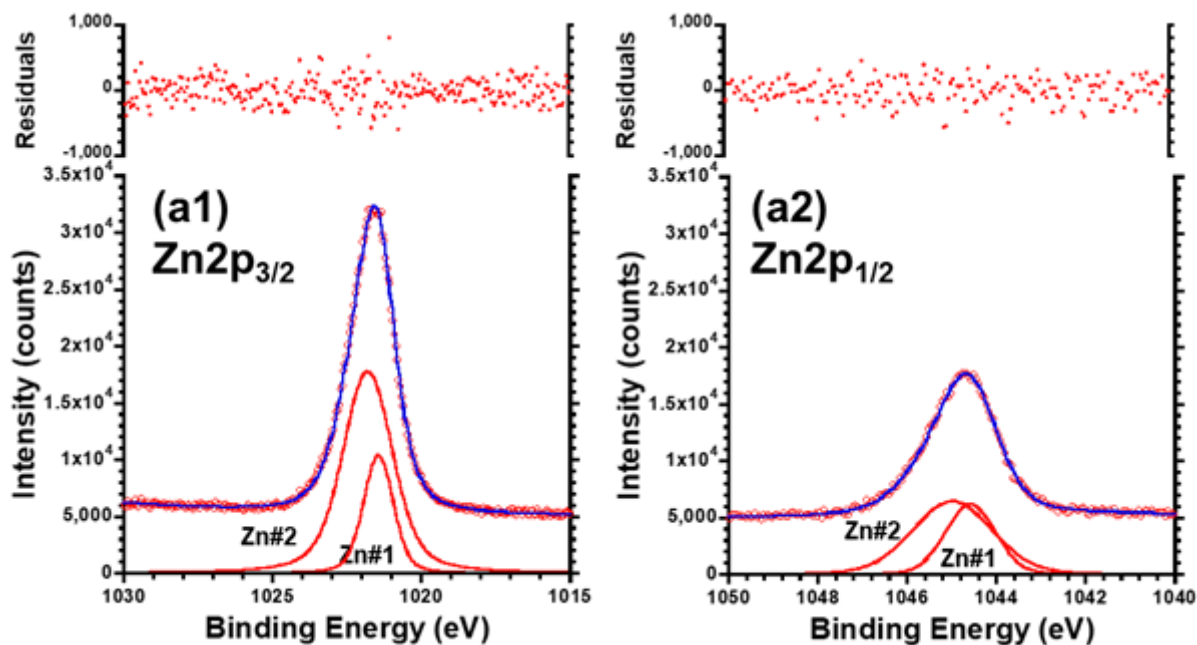O 1s XP spectra of (a) CGO2 and (b) CZ4.

Figure 10

Zn 2p XP spectra of CZ4.

Supplementary Files

This is a list of supplementary files associated with this preprint. Click to download.

- SupportingInformationChoiHayakawaSciRep.docx